npj | quantum information

Article

Published in partnership with The University of New South Wales

https://doi.org/10.1038/s41534-025-01014-z

Quantum-enhanced imaging for characterizing anisotropic material

Meng-Yu Xie[1,2,4], Su-Jian Niu[1,2,3,4], Zhao-Qi-Zhi Han[1,2], Yin-Hai Li[1,2], Ren-Hui Chen[1,2], Xiao-Hua Wang[1,2], Ming-Yuan Gao[1,2], Li Chen[1,2], Yue-Wei Song[1,2], Zhi-Yuan Zhou[1,2] ✉ & Bao-Sen Shi[1,2] ✉

Polarimetric imaging, a technique that captures the invisible polarization-related properties of given materials, has broad applications from fundamental physics to advanced fields such as target recognition, stress detection, biomedical diagnosis and remote sensing. The introduction of quantum sources into classical imaging systems has demonstrated distinct advantages, yet few studies have explored their combination with polarimetric imaging. In this study, we present a quantum polarimetric imaging system that integrates polarization-entangled photon pairs into a polarizer-sample-compensator-analyzer-typed polarimeter. Our system visualizes the birefringence properties of a periodical-distributed anisotropic material under decreasing illumination levels and diverse disturbing light sources. Compared to the classical system, the quantum approach reveals the superior sensitivity and robustness in low-light conditions, particularly useful in biomedical studies where the low illumination and non-destructive detection are urgently needed. The study also highlights the nonlocality of entangled photons in birefringence measurement, indicating the potential of quantum polarimetric system in the remote sensing domain.

Polarization, one of the fundamental properties of light, exhibits various physical features of the tested specimen that are invisible to the human eye. The polarimetric imaging technique is used to visualize these polarization-related properties of the imaged objects or media. It can be used to enhance the contrast between the background and the target, which is difficult to distinguish in conventional imaging[1]. It also provides a way to measure invisible parameters undetectable by conventional imaging, such as optical constants[2], chiral properties[3], and stress/strain distributions[4,5]. Nowadays, polarimetric imaging has been widely used for a variety of practical scenarios, such as 3D shape reconstruction[6,7], solar and atmospheric phenomena[8], terrestrial vegetation and ocean detection[9,10], biomedical diagnosis[11,12], navigation[13] and so on.

The introduction of a quantum light source into conventional imaging opens up a new way to enhance the measurement accuracy especially in low illumination fields[14,15]. The ability to break the standard quantum limit has been substantiated both theoretically and experimentally, demonstrating great promise for the field of metrology[16,17]. Furthermore, the nonlocal properties of the entangled photon source facilitate the separation of the control and measurement processes[18], a feature of great value in the field of remote sensing applications. So far, the mainstream of the quantum imaging work focuses on accurately measuring the external morphology of the tested sample[19]. The "invisible" polarization-correlated quantum imaging has only a limited amount of research, and most of them are single-spot detection of the homogeneous materials[20–22]. The works combining the polarimetric imaging and quantum imaging are extremely rare[23], and the corresponding researches are still remained to be explored.

In this work, we introduce polarization entangled photon pairs into a polarizer-sample-compensator-analyzer-typed polarimeter to form a two-dimensional quantum polarimetric imaging system. An anisotropic material with periodically distributed birefringence properties is selected as the sample to be imaged under diminishing illumination intensity and different sources of disturbance light. By comparing the classical and quantum polarimeters under the same conditions, we use the structural similarity index (SSIM) to quantitatively show the minimum measurable source intensity and the impact of stray light on both systems. Furthermore, we exploit the nonlocality inherent in entangled photon sources to remotely adjust the polarization state incident on the sample, which allows us to extract birefringence information without any interference on the measurement arm.

Unlike the aforementioned experimental works on quantum polarimetry, our experiment performs a two-dimensional anisotropic material characterization instead of the single-spot polarization measurement for the

[1]Key Laboratory of Quantum Information, University of Science and Technology of China, Hefei, Anhui, 230026, China. [2]Synergetic Innovation Center of Quantum Information & Quantum Physics, University of Science and Technology of China, Hefei, Anhui, 230026, China. [3]Xinjiang Key Laboratory for Luminescence Minerals and Optical Functional Materials, School of Physics and Electronic Engineering, Xinjiang Normal University, Urumqi, Xinjiang, 830054, China. [4]These authors contributed equally: Meng-Yu Xie, Su-Jian Niu. ✉e-mail: zyzhouphy@ustc.edu.cn; drshi@ustc.edu.cn

homogeneous materials, and further provides a direct and intuitive comparison between the quantum polarimetric imaging system and its classical counterpart, demonstrating its abilities to accurately characterize birefringent properties under extremely low illumination, leveraging its distinctive non-locality for the remote manipulation of measurements, and exhibiting its robustness to efficiently shield the impact of stray light perturbation. Our system differs from classical quantum polarimeter mainly for the unique and useful non-local properties, the entanglement in polarization, as well as the correlations in the time/frequency and spatial degrees of freedom, allows various applications in the measurement of photosensitive materials, active biological samples and remote monitoring scenarios.

Results

The experimental setup of the quantum polarimetric imaging system is shown in Fig. 1. It consists of three main parts: An entangled photon source part for the generation of polarization-entangled photon pairs based on the Sagnac interferometer configuration[24] and the spontaneous parametric down conversion of a type-II phase-matched periodically poled $KTiOPO_4$ (PPKTP) crystal. A sample measurement part that allows photon-sample interaction and collecting the polarimetric information using the raster scanning method[15]. Note that a QWP, whose optical axis angle is always parallel to the input photon polarization, is introduced after the target sample. This technique is called the Senarmont compensation method, and the advantages for this technique can be found in our previous work[25], or in the Supplementary Materials (A). Two polarization analysis parts used for each of the separated photon pairs in both the upper control path and the lower measurement path for polarization base selection and joint measurement.

Before analyzing unknown samples using the above experimental setup, we initially assess the entangled photon source and calibrate our quantum polarimetric imaging system using a commercially available quarter wave plate (QWP). In the calibration process, we introduce the conventional four-step phase-shifting method and further improve it to calculate the phase retardance and optical axis angle of each pixel here and in all the following experiments. The system accuracy is defined as the deviation between the images captured by our quantum polarization measurement system and the standard reference images obtained from a commercial automatic polarimeter whose retardance measurement accuracy is within ±1 nm. After the careful calibration, the system can achieve a nanometer-level accuracy in phase retardance measurements and ensuring an accuracy within 1° for the angle of optical axis, feasible for imaging the 2D inhomogeneous anisotropic samples in the following sections.

The details of the experiment configuration, the improved four-step phase-shifting calculation method and the entire calibration process can be found in the following Materials and methods section and further in the Supplementary Materials (B–D).

Polarimetric imaging under low illumination

In this section, the sample is a polymer depolarizer characterized by a periodic birefringence pattern. Under conditions of extremely low illumination, we record the phase retardances and optical axis orientations obtained by both quantum and classical imaging setups. The comparative outcomes are shown in Fig. 2.

Figure 2 illustrates the phase retardance and optical axis angle measurements for the polymer depolarizer across an imaging area of 2.5mm × 2.5mm. Utilizing a 0.25 mm incremental movement in two orthogonal directions, we capture a total of 11 × 11-pixel images in each measurement. For each pixel, we collect the coincidence photon pairs with a 1.6 ns coincidence window and 1 s acquisition time. The left two columns present the results from a quantum imaging system using local operations, specifically by rotating the HWP right after the sample in the measurement arm, while maintaining a fixed position for the HWP on the control side to determine the polarization state of the input photons. The HWP in the deep purple box of Fig. 1 is temporarily removed for these measurements. The middle two columns display the results from a classical imaging system. Notably, the transformation of the measurement arm into a classical polarimeter is achieved by inserting an additional HWP (as indicated in the deep purple box) ahead of the focal lenses, thereby altering the polarization of the input photons. Consequently, variations in the single photon count at different HWP orientations provide valid information for the sample's birefringence properties.

Comparing the measurement results depicted in Fig. 2, it is evident that both systems exhibit comparable trends and periodic pattern for the tested sample. However, as the input intensity decreases, the classical system shows a noticeable deviation from the original result. From 2×10^4 cps to 2×10^3 cps, the maximum and minimum values remain the same, while the width of the peaks gradually increases. Upon further reduction of the input intensity to 1×10^3 cps, the phase retardance value appears a significant

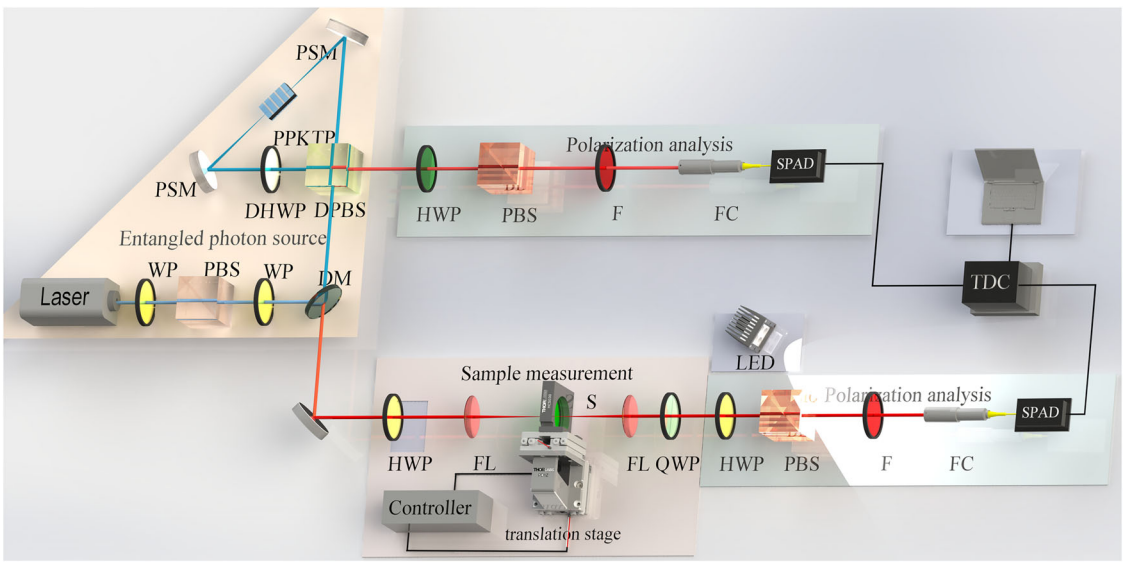

Fig. 1 | Experimental setup. Entangled photon source part: WP, waveplate set, including a quarter wave plate and a half wave plate (HWP); PBS, polarizing beam splitter; DM: dichroic mirror; DPBS, dichroic PBS; DHWP, dichroic HWP; PSM, off-axis parabolic silver mirror; PPKTP, periodically poled KTP crystal; Sample measurement part: Motorized translation stage; FL, focal lens; S, sample. Polarization analysis part: F, filter; FC, fiber collimator. SPAD, Single-photon Avalanche Diode. TDC, Time-to-digital converter.

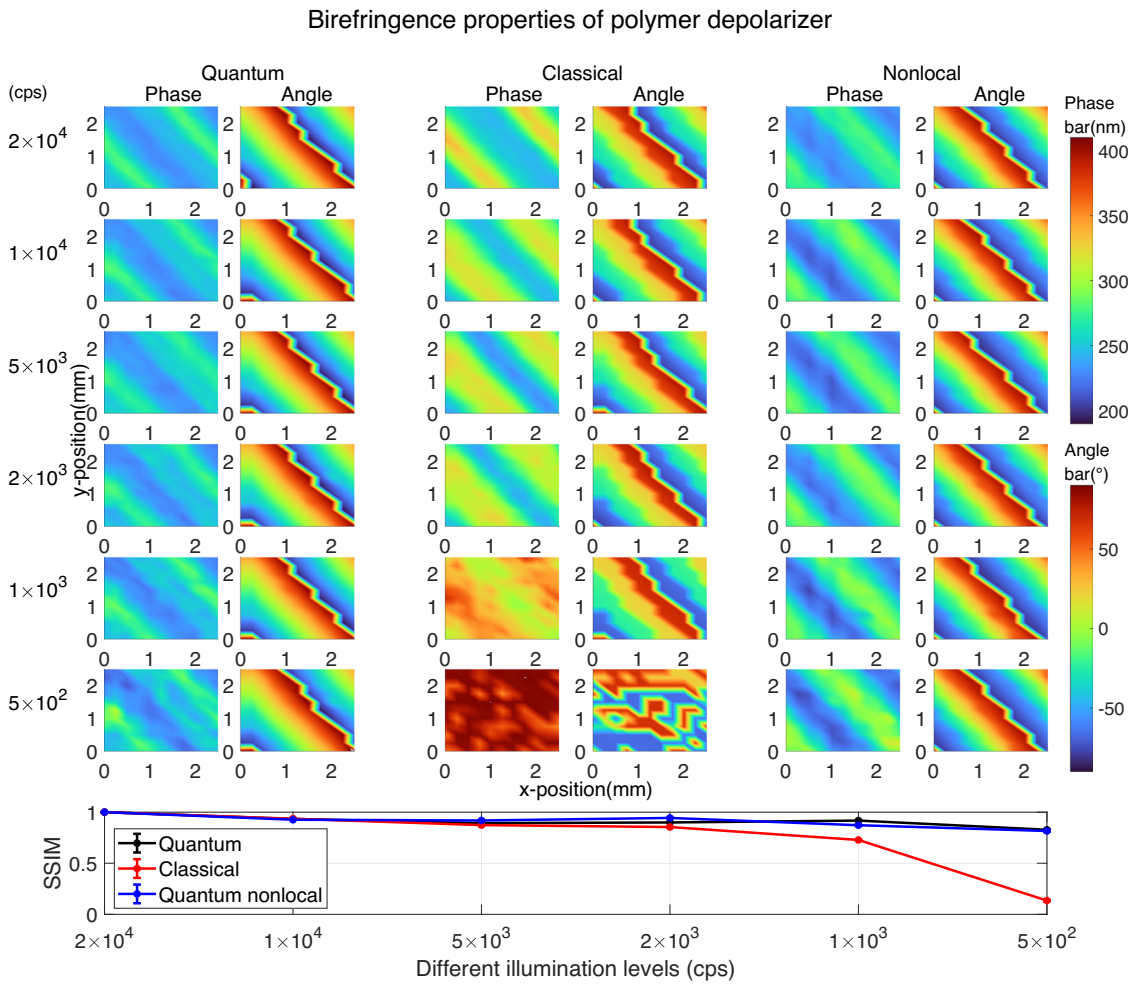

Fig. 2 | Phase retardance and optical axis angle under different input illumination. The left numbers show the input photon numbers for the images in the same row. The left, middle and right two columns show the phase retardance and the optical axis angle measured by the quantum imaging system with local operation, the classical imaging system and the quantum system with nonlocal operation, respectively. The bottom sub-figure shows the SSIM of each phase retardation image.

deviation from its initial value. And the periodic pattern completely disappeared for both phase retardance and optical axis angle when the input intensity reduces to 5×10^2 cps. In contrast, the quantum system consistently demonstrates high fidelity in both shape and value from 2×10^4 cps to 5×10^2 cps.

To quantify the above qualitative analysis and to define the imaging accuracy of both systems, we compare the measurement results of the quantum measurement system with the reference image pixel-by-pixel. In between, the SSIM (Structural Similarity) is considered as the image quality assessment metric. It provides a normalized measurement of the similarity in average detection intensity and contrast between two images, which is more closely aligned with human visual perception, thus making it more suitable for assessing the similarity of images with certain structural shapes. The calculation formula is[26]

$$\mathrm{SSIM} = \frac{(2\mu_x\mu_y + \mathrm{C}_1)(2\sigma_{xy} + \mathrm{C}_2)}{(\mu_x{}^2 + \mu_y{}^2 + \mathrm{C}_1)(\sigma_x{}^2 + \sigma_y{}^2 + \mathrm{C}_2)}. \quad (1)$$

Where $\mu_{x(y)}$, $\sigma_{x(y)}$ and σ_{xy} represents the average, standard deviation and covariance of the two compared images, respectively. $C_1 = C_2 = 0$ when $\mu_x{}^2 + \mu_y{}^2$ or $\sigma_x{}^2 + \sigma_y{}^2$ are far from zero. This definition provides a normalized accuracy estimate, with values closer to 1 indicating that the estimated image is closer to the reference image. At the same time, considering the imprecision caused by quantum fluctuation, we calculate the standard deviation of each SSIM, which reflects the precision of our measurement system.

The calculated results are illustrated in the bottom inset of Fig. 2. Regarding the images measured with the maximum intensity as the reference, the SSIMs of other images captured from the quantum polarimetric imaging system are 0.9336 ± 0.0002, 0.8926 ± 0.0012, 0.8989 ± 0.0014, 0.9171 ± 0.0009 and 0.8270 ± 0.0021 for the photon levels from 1×10^4 cps to 5×10^2 cps, respectively. As a comparison, the classical system's SSIM progressively declines as the input intensity decreases. The values are shown to be 0.9353 ± 0.0004 for 1×10^4 cps, 0.8742 ± 0.0004 for 5×10^3 cps, 0.8544 ± 0.0009 for 2×10^3 cps, 0.7279 ± 0.0031 for 1×10^3 cps and 0.1348 ± 0.0067 for 5×10^2 cps. Compared with the quantum system whose average SSIMs are all above 0.8, the classical system shows a steadily decreasing when the photons gradually reduced from 2×10^4 cps to 1×10^3 cps, and finally has an obvious deterioration with 5×10^2 cps input photons. Meanwhile, the standard deviation of SSIMs in the quantum and classical measurements are basically within the same order of magnitude. Only when the classical images are almost indistinguishable amidst the noise, the precision shows an obvious difference compared with quantum system. This phenomenon is mainly because of the entanglement-assisted configuration in the quantum system, where only one photon in the pair is passing through the sample while the other serves as the ancilla bit. It has been demonstrated theoretically that the entanglement-assisted system has no enhancement on the precision limit, but has advantages in estimating

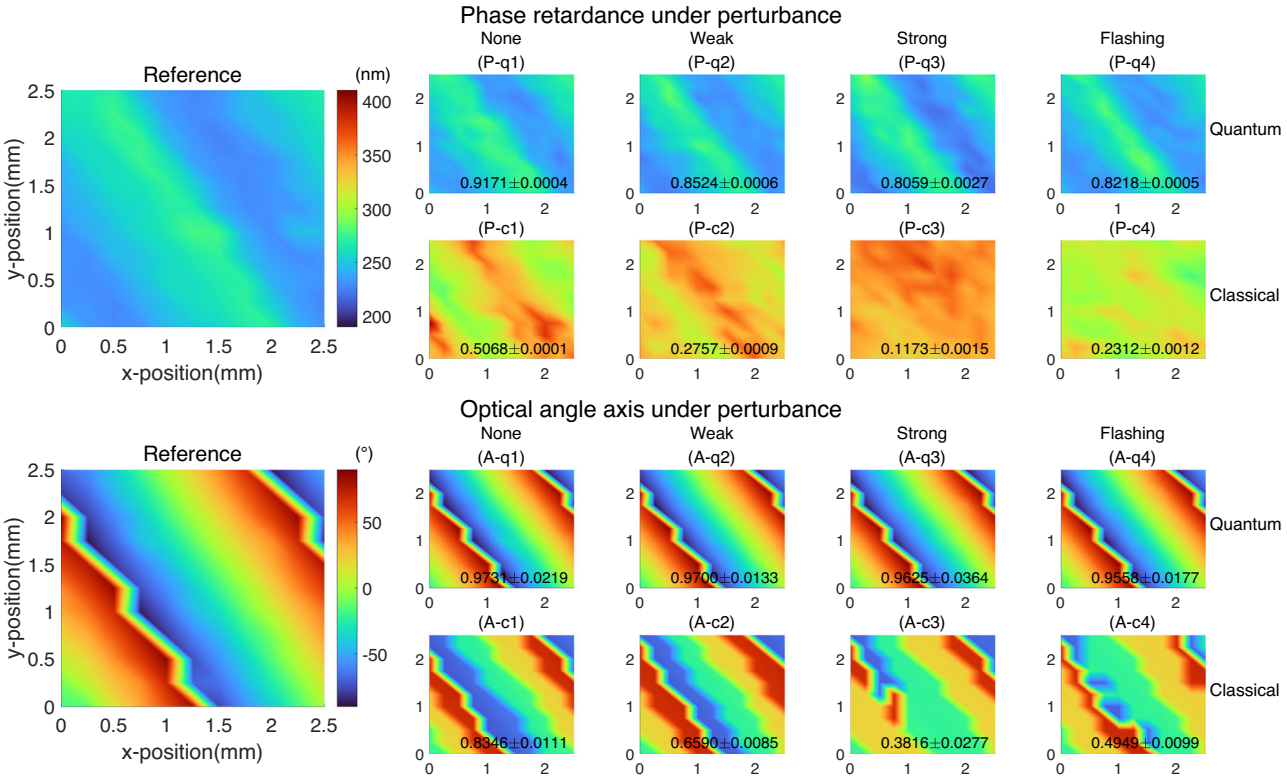

Fig. 3 | Phase retardance and optical axis angle under perturbance. The left subplot (Reference) presents the measurement outcomes under 2×10^4 cps conditions without any interference. In contrast, the remaining subplots depict measurements conducted at a 1×10^3 cps illumination level. **(P/A-q1) to (P/A-q4):** Illustrate the phase retardance/the optical axis angle obtained by the quantum system, under conditions of no perturbation, weak perturbation, strong perturbation, and flashing perturbation, respectively. **(P/A-c1) to (P/A-c4):** Obtained by the classical system under the same conditions as quantum system.

channel-correlated parameters in a non-ideal transmission channel compared to the coherent state input[27,28].

Based on the above comparison, the quantum polarimetric imaging system shows apparent advantages in enhancing the measurement accuracy and maintains better measurement precision under extremely low-illumination conditions.

Nonlocality

As a unique feature of entangled photon pairs, we also show the nonlocality of photons when measuring sample birefringence. The corresponding results under varying illumination conditions are presented in the right two columns of Fig. 2. Compared with the experimental configuration depicted in Fig. 1, we have relocated the QWP compensator to the control arm and adjusted the angle of HWP within the control arm for each measurement. Consequently, without any changes in the measurement arm, we are able to obtain the phase retardance and optical axis angle of the sample located in the measurement arm by only adjusting the components in the control side.

The results of the quantum nonlocal test show similar trends to those of the quantum local experiment. As evidenced by the images in Fig. 2, the phase retardance and the optical axis angle exhibit very little sensitivity to diminishing illumination levels. When the input photon number gradually decreases from 1×10^4 cps to 5×10^2 cps, the SSIMs are shown to be 0.9258 ± 0.0011, 0.9184 ± 0.0019, 0.9434 ± 0.0020, 0.8720 ± 0.0045 and 0.8153 ± 0.0082, respectively. Moreover, the remote-control capability offers distinct advantages over the quantum local experiment by significantly minimizing the disturbance to the measurement arm. This feature suggests promising applications in specialized environments, including but not limited to the remote sensing and biomedical diagnostics.

Polarization imaging under perturbance

In this section, we introduce an interference light source to investigate the robustness of quantum polarimetric imaging under conditions of perturbation. A light-emitting diode (LED) in the measurement arm, as depicted in Fig. 1, operates in three distinct illumination modes: weak illumination (50 lm), strong illumination (150 lm) and intermittent flashing mode. In between, the intermittent flashing mode is that the white LED light switches between strong brightness (150 lm) and off at a constant interval. In strong illumination mode, the LED can introduce approximately 2×10^3 cps of additional stray photons for single arm detection. In order to introduce enough perturbance, we decrease the measurement illumination to the same level, i.e. 1×10^3 cps, to compare the performance of two systems. The comparative analysis of the systems' performance is presented in Fig. 3.

Figure 3 presents the birefringence property variations of the polymer depolarizer under three distinct types of perturbation. The imaging area, which remains at 2.5 mm × 2.5 mm with a total of 11 × 11 pixels, differs from the area analyzed in the previous section. The first row of images corresponds to the results obtained from the quantum polarimetric imaging system. It is observed that all four images exhibit a high degree of consistency. The average SSIM values and the standard deviations, indicated in the lower corners of each image, are all above 0.8. Specifically, they are 0.9171 ± 0.0004 for the none perturbation mode, 0.8524 ± 0.0006 for the weak perturbation mode, 0.8059 ± 0.0027 for the strong perturbation mode and 0.8218 ± 0.0005 for the flashing perturbation mode, signifying excellent agreement with the reference.

In contrast, the second row displays the results from the classical system, which exhibit variability in both values and patterns. Notably, the measurement under zero perturbation already deviates from the reference (0.5068 ± 0.0001), consistent with the result shown in the row 1×10^3 cps of Fig. 2. The presence of perturbation further degrades the detection

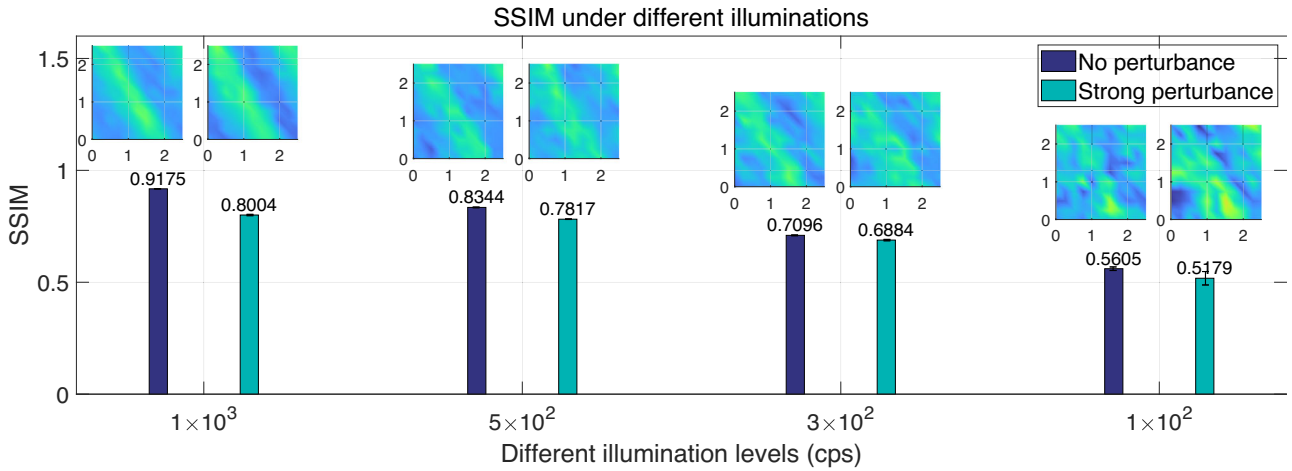

Fig. 4 | Comparison of SSIMs in unperturbed and strong-perturbed environments. The left bar in each group represents the SSIM values obtained under unperturbed conditions for 1×10^3, 5×10^2, 3×10^2, 1×10^2 cps input illuminations, respectively. Right bar of each group shows the SSIM with strong perturbance under the same illuminations.

outcomes. Specifically, the SSIM values for the phase retardances decline to 0.2757 ± 0.0009 for weak perturbation, 0.1173 ± 0.0015 for strong perturbation, and 0.2312 ± 0.0012 for flashing perturbation, indicating a significant reduction in similarity to the reference image.

Based on the above data and images, the average SSIM values demonstrate that the quantum images have stronger resistance towards the stray-light-induced image deterioration, thus maintaining high accuracy under a noise environment. One thing that need to be further discussed is that the accuracy (average SSIM) of the angle measurement seems to be higher than that of the retardance measurement, while the precision (standard deviation) is lacking under same conditions. The reason lies in the calculation method stated in the Supplement Materials (C), in which we identify the quadrant of the optical angle θ based on the sign of $\sin 2\theta$ and $\cos 2\theta$ to extend the measurement range from $2\theta \in [0, \pi]$ to $[0, 2\pi]$. This extension is crucial for accurately measuring the current sample, as the variation of the optical axis is periodically distributed within $2\theta \in [0, 2\pi]$, and utilizing the original four-step phase-shifting method would introduce errors in both the range and the number of cycles for the optical axis angle distribution. With the improved four-step phase-shifting method, we can recognize a general trend of the angle variation by determining the quadrant in which the angle lies. This trend contributes a portion of the structural similarity, thus induce higher SSIM average values in the angle measurement compared to that of the retardance measurement. However, also because of this method, when the value of $\sin 2\theta$ and $\cos 2\theta$ are close to zero, a small variation would cause an obvious numerical change, causing a deterioration in the measurement precision. The above analysis shows that the differences in SSIM values between the angles and the retardance are all attributed to the new calculation method introduced to resolve the multi-valued issue of the angle measurement. Noted that this method has the same effects on both classical and quantum systems, therefore has no influence on their performance comparison when measuring the same parameter. Besides, we tend to use the SSIM values calculated from the retardance measurement rather than the angle measurement as the representation of the system performance in the low-illumination environment, since the retardance measurement does not need to deal with the multi-valued problem and shows a more intuitive distribution changes caused by the perturbance or the decreasing input photons.

Given that the perturbations examined so far have not yet revealed the limitations of the quantum system, we have conducted an additional investigation focusing solely on the quantum system. Due to the fixed mode intensity of the interference source, which prevents us from further increasing the perturbance level, we have opted to reduce the intensity of the photon source instead. This approach allows us to further compare the measurement results between an unperturbed environment and a strongly perturbed scenario for the quantum system.

Figure 4 illustrates that the periodic distribution characteristic of the sample diminishes as the input illumination decreases to 100 photons per second. The bars at the left side of each group show the retardance measurement results with no perturbance while the right bars are obtained when the measurement arm is exposed to the strong perturbance. The average values and standard deviations of the bars are shown to be 0.9175 ± 0.0005 and 0.8004 ± 0.0029 for 1000 photons incidence, 0.8344 ± 0.0014 and 0.7817 ± 0.0012 for 500 photons incidence, 0.7096 ± 0.0016 and 0.6884 ± 0.003 for 300 photons incidence, 0.5605 ± 0.008 and 0.5179 ± 0.03 for 100 photons incidence. As the light source intensity decreases, the average SSIM values of the measured images gradually decreases, while the corresponding standard deviation shows an upward trend. This suggests that a reduction in signal intensity leads to a decrease in both the accuracy and precision of measurements taken under noisy conditions, which aligns with the intuitive inference. Moreover, even with an incidence of 100 photons, the SSIM remains above 0.5, which is significantly higher than the classical case where the SSIM drops to 0.1348 with an incidence of 500 photons (Fig. 2), showing a significant advantage in measurement accuracy under low-light conditions. Notably, the strong perturbation at 150 lm has a negligible impact on the measurements obtained by the quantum polarimetric system across all input levels. This resilience can be attributed to the dual-path structure of the quantum system, where the coincidence photon detection mechanism demonstrates a high degree of perturbance resistance due to the presence of an unperturbed control arm. In fact, it is noted that even when both arms are subjected to perturbance simultaneously, as long as the stray light enters the reference and measurement arm with a time difference larger than the coincidence window (1.6 ns), the system still has the ability to resist these perturbances.

Discussion

In summary, we build a quantum polarimetric imaging system to measure the birefringence properties of anisotropic samples with high accuracy under low illumination conditions. By combining an improved four-step phase shift method with the Senarmont compensation technique, our system achieves nanometer-level accuracy in phase retardance measurement and 1° for the optical axis angle measurement. Taking a periodically distributed polymer depolarizer as a sample, we compare the image quality between the quantum system and its classical counterpart over a range of decreasing illumination levels. Besides, we also investigate the impact of different perturbation modes on the obtained images and explore the unique nonlocal property of the quantum system.

The results show that quantum system has higher sensitivity, enabling it to accurately detect samples even at significantly lower input illumination levels, down to as few as 100 photons per second. As the input illumination gradually reduces from 2×10^4 cps to 5×10^2 cps, the SSIM for each measurement in the quantum system remains consistently high, exceeding a similarity of 0.8. In contrast, the classical system experiences an obvious decline in performance at 1×10^3 cps and retrieve to 0.1348 with a 5×10^2 cps input. Furthermore, the quantum system demonstrates enhanced robustness against stray-light-noise compared to the classical system. It can feasibly resist perturbations from various interference modes, ranging from strong (150 lm) to weak (50 lm) perturbance, with only minimal degradation (≤0.1) in SSIM. While the classical system suffers a deterioration of 0.39 in SSIM for strong perturbance and 0.23 for weak perturbance.

Our experiment highlights the quantum polarimetric imaging system with its dual-way structure and coincidence measurement, which efficiently shields against background noise and perturbations affecting the single-arm. This design significantly enhances the signal-to-noise ratio, greatly improving the accuracy and noise resistance of the birefringence measurements under low-illumination measurement. The future development of the experimental system aims to extend its measurement capabilities to more complex media and to enhance imaging quality and efficiency by increasing photon source intensity and by utilizing imaging single-photon detector arrays.

Our quantum polarization imaging system, combining the strengths of quantum and polarization imaging, offers unique advantages in multiple fields. For example, it enables non-destructive, high-precision detection for the photosensitive thin-film materials under weak light conditions, mainly focusing on the polarization-correlated properties such as optical anisotropy, surface roughness and stress distribution. In biomedical field, it provides more detailed information on pathological tissues through polarization-sensitive detection, supporting low-light, non-invasive diagnostics and provided non-local remote control to against the possibly inaccessible and complex environment. Additionally, in air-to-ground target detection, it enhances target recognition in complex environments by leveraging material-specific polarization responses and the robustness of quantum imaging against atmospheric disturbances. These applications stress the unique non-locality and interference resistance properties of our system, demonstrating its great potential for high-accuracy polarimetric characterization in low illumination environments.

Materials and methods

Experimental configuration

A 405 nm continuous wave diode laser (Kunteng Quantum Technology Co. Ltd) with a 45° linear polarization enters the central dichroic polarizing beam splitter (DPBS) of the Sagnac interferometer. The split horizontal and vertical polarized light pass clockwise and counterclockwise through the loop, which is formed by two symmetrical parabolic silver mirrors (PSM) and a 45° tilted dichroic half-wave plate (DHWP). Each of the bidirectional light pumps a type-II phase-matched PPKTP crystal (Raicol Crystals Ltd.) to generate the orthogonally polarized photon pairs by the spontaneous parametric down conversion. Then the central DPBS recombines the correlated photon pairs to form the polarization-entangled photon source.

In the sample measurement part, a two-dimensional motorized translation stage is used to move the sample precisely with a minimal step size of 0.2 μm. Two plano-convex lenses with focal lengths of 50 mm focus the light onto the sample surface. The raster scanning technique, although more time consuming, is used for the 2D imaging because of the higher signal-to-noise ratio (SNR) compared with the full-field imaging technique[29]. After the sample measurement part, we use a QWP as a compensator to improve the performance of the system, the benefit of which has been analyzed in the **Supplementary Material**.

Both the control and measurement arms have the same configuration of collection components, i.e. a true zero-order half wave plate (HWP) for base selection, an 808 nm PBS for projective measurement, a long pass filter and a bandpass filter to remove the pump light. The emitted photons are then collected in a single-mode fiber and detected by a single-photon avalanche diode (Excelitas, SPCM-AQRH) with a detection efficiency of approximately 60% at a wavelength of 810 nm.

Calculation method

We use the improved four-step phase-shifting method to derive the sample's birefringence information from coincidence photon counts. Following the experimental setup in Fig. 1, the output coincidence counts for the joint measurement of control and measurement arms are:

$$\begin{aligned} N &= N_0 |tr(\hat{E}_c \otimes \hat{E}_m (\hat{J}_c \otimes \hat{J}_m)|\phi\rangle_{cm}\langle\phi|)|^2 \\ &= \tfrac{N_0}{4}\{1 - \sin\delta \sin(4h_m - 2q)\sin(4h_c + 2\theta) + \cos(4h_m - 2q) \\ &\times [-\cos(2q - 2\theta)\cos(4h_c + 2\theta) + \cos\delta \sin(2q - 2\theta)\sin(4h_c + 2\theta)]\}. \end{aligned} \tag{2}$$

Here, the subscripts c and m stand for the control and measurement arm, while h and q represent the angle of HWP and QWP, respectively. $|\phi\rangle_{cm} = 1/\sqrt{2}[|HV\rangle + |VH\rangle]$ is the initial entangled photon state generated by the Sagnac interferometer. $\hat{J}_{c(m)}$ is the evolution operator of the photons in the control (measurement) arm. Based on the experimental setup, we have $\hat{J}_c = I$ and $\hat{J}_m = \hat{U}_{QWP}(q)\hat{U}_{sample}(\delta, \theta)$, where δ and θ stand for the phase retardance and optical axis angle of the tested sample. Base selection and projective measurement are contained in the projective operator $\hat{E}_{c(m)}$ with HWP angle set to $h_{c(m)}$ in the control (measurement) arm.

Based on Eq. (2), the birefringence parameters δ and θ can be calculated by varying the controllable $h_{c(m)}$ to get its corresponding coincidence counts. The conventional four-step phase-shifting method selects four angles for the analyzer, i.e., 0°, 45°, 90° and 135°, to derive the birefringence parameters. However, the range of the detectable optical angle θ is usually limited to $[0, \pi/2]$. To meet the requirements of our anisotropic sample, which has an optical axis angle varying from 0 to π, we improve the conventional four-step phase-shifting method by performing the method twice in both H-base (h_c= 45°) and D-base ($h_c = 22.5°$) in the quantum polarimetric imaging system. In this way, we are able to extend the measurable range from $[0, \pi/2]$ to $[0, \pi]$. Further calculation details are showed in the Supplementary Materials (C).

Data availability

All data needed to evaluate the conclusions in the paper are present in the paper and/or the Supplementary Materials.

Received: 28 August 2024; Accepted: 20 March 2025;
Published online: 04 April 2025

References

1. Liang, J., Ren, L., Qu, E., Hu, B. & Wang, Y. Method for enhancing visibility of hazy images based on polarimetric imaging. *Photonics Res.* **2**, 38–44 (2014).
2. Yim, C. et al. Investigation of the optical properties of MoS2 thin films using spectroscopic ellipsometry. *Appl. Phys. Lett.* **104**, 103114 (2014).
3. Schulz, M. et al. Giant intrinsic circular dichroism of prolinol-derived squaraine thin films. *Nat. Commun.* **9**, 2413 (2018).
4. Doualle, T., Ollé, A., Cormont, P., Monneret, S. & Gallais, L. Laser-induced birefringence measurements by quantitative polarized-phase microscopy. *Opt. Lett.* **42**, 1616–1619 (2017).
5. Mikami, N., Nagao, C., Sawada, T. & Sato, K. Measurement of Stress Induced Birefringence of Bi12GeO20 Single Crystals by a New Ellipsometry. *Jpn. J. Appl. Phys.* **26**, 152 (1987).
6. Han, P. et al. Computational polarization 3D: New solution for monocular shape recovery in natural conditions. *Opt. Lasers Eng.* **151**, 106925 (2022).

7. Li, X., Liu, F., Han, P., Zhang, S. & Shao, X. Near-infrared monocular 3D computational polarization imaging of surfaces exhibiting nonuniform reflectance. *Opt. Express* **29**, 15616–15630 (2021).
8. Roger, J. C., Santer, R., Herman, M. & Deuzé, J. L. Polarization of the solar light scattered by the earth-atmosphere system as observed from the U.S. shuttle. *Remote Sens. Environ.* **48**, 275–290 (1994).
9. Liu, S., Lin, Y., Yan, L. & Yang, B. Modeling Bidirectional Polarization Distribution Function of Land Surfaces Using Machine Learning Techniques. *Remote Sens* **2020**, 3891 (2020).
10. Schechner, Y. Y. & Karpel, N. Recovery of underwater visibility and structure by polarization analysis. *IEEE J. Ocean. Eng.* **30**, 570–587 (2005).
11. He, C. et al. Polarisation optics for biomedical and clinical applications: a review. *Light Sci. Appl.* **10**, 194 (2021).
12. Novikova, T., Meglinski, I., Ramella-Roman, J. C. & Tuchin, V. V. Special section guest editorial: polarized light for biomedical applications. *J. Biomed. Opt.* **21**, 71001 (2016).
13. Li, Q. et al. Polarimetry for bionic geolocation and navigation applications: a review. *Remote Sens* **15**, 3518 (2023).
14. Jost, B. M., Sergienko, A. V., Abouraddy, A. F., Saleh, B. E. A. & Teich, M. C. Spatial correlations of spontaneously down-converted photon pairs detected with a single-photon-sensitive CCD camera. *Opt. Express* **3**, 81–88 (1998).
15. Pittman, T. B., Shih, Y., Strekalov, D. V. & Sergienko, A. V. Optical imaging by means of two-photon quantum entanglement. *Phys. Rev. A* **52**, R3429–R3432 (1995).
16. Jakeman, E. & Walker, J. G. Analysis of a method for the generation of light with sub-poissonian photon statistics. *Opt. Commun.* **55**, 219–222 (1985).
17. Jakeman, E. & Rarity, J. G. The use of pair production processes to reduce quantum noise in transmission measurements. *Opt. Commun.* **59**, 219–223 (1986).
18. Strekalov, D. V., Sergienko, A. V., Klyshko, D. N. & Shih, Y. H. Observation of two-photon "ghost" interference and diffraction. *Phys. Rev. Lett.* **74**, 3600–3603 (1995).
19. Moreau, P.-A., Toninelli, E., Gregory, T. & Padgett, M. J. Imaging with quantum states of light. *Nat. Rev. Phys.* **1**, 367–380 (2019).
20. Restuccia, S., Gibson, G., Cronin, L. & Padgett, M. Measuring optical activity with unpolarized light: Ghost polarimetry. *Phys. Rev. A* **106**, 062601 (2022).
21. Tischler, N. et al. Quantum optical rotatory dispersion. *Sci. Adv.* **2**, e1601306 (2016).
22. Yoon, S.-J., Lee, J.-S., Rockstuhl, C., Lee, C. & Lee, K.-G. Experimental quantum polarimetry using heralded single photons. *Metrologia* **57**, 045008 (2020).
23. Zhang, Y. et al. Quantum imaging of biological organisms through spatial and polarization entanglement. *Sci. Adv.* **10**, eadk1495 (2024).
24. Li, Y., Zhou, Z.-Y., Ding, D.-S. & Shi, B.-S. CW-pumped telecom band polarization entangled photon pair generation in a Sagnac interferometer. *Opt. Express* **23**, 28792–28800 (2015).
25. Xie, M.-Y. et al. Quantum entanglement enabled ellipsometer for phase retardance measurement. **23**, https://doi.org/10.48550/arXiv.2402.17401 (2024).
26. Wang, Z., Bovik, A. C., Sheikh, H. R. & Simoncelli, E. P. Image quality assessment: from error visibility to structural similarity. *IEEE Trans. Image Process.* **13**, 600–612 (2004).
27. Huang, Z., Macchiavello, C. & Maccone, L. Usefulness of entanglement-assisted quantum metrology. *Phys. Rev. A* **94**, 012101 (2016).
28. Demkowicz-Dobrzański, R. & Maccone, L. Using entanglement against noise in quantum metrology. *Phys. Rev. Lett.* **113**, 250801 (2014).
29. Zhang, L., Neves, L., Lundeen, J. & Walmsley, I. A characterization of the single-photon sensitivity of an electron multiplying charge-coupled device. *J. Phys. B:. Mol. Opt. Phys.* **42**, 114011 (2009).

Acknowledgements

Sincerely thanks for the technical support of Suzhou PTC Optical Instrument Co., Ltd. This work is supported by the National Key Research and Development Program of China (2022YFB3607700, 2022YFB3903102), National Natural Science Foundation of China (NSFC) (11934013, 92065101, 62005068), Innovation Program for Quantum Science and Technology (2021ZD0301100), Space Debris Research Project of China (No. KJSP2020020202), Postdoctoral Fellowship Program of CPSF (GZC20232559) and USTC Research Funds of the Double First-Class Initiative.

Author contributions

Conceptualization: ZYZ, BSS. Theoretical calculation: MYX, SJN. Experimental design: MYX, SJN. Experimental construction: MYX, SJN, ZQZH, RHC. Device fabrication: YHL, ZYZ, BSS. Optical and device characterization: XHW, MYG, LC, YWS. Writing—original draft: MYX. Writing—review & editing: MYX, SJN, ZYZ, BSS.

Competing interests

The authors declare no competing interests.

Additional information

Supplementary information The online version contains supplementary material available at https://doi.org/10.1038/s41534-025-01014-z.

Correspondence and requests for materials should be addressed to Zhi-Yuan Zhou or Bao-Sen Shi.